

Photo-Induced Schottky Barrier Lowering in 2D Monolayer WS₂ Photodetectors

*Ye Fan, Yingqiu Zhou, Xiaochen Wang, Haijie Tan, Youmin Rong, and Jamie H. Warner**

¹Department of Materials, University of Oxford, Parks Road, Oxford, OX1 3PH, United Kingdom

*jamie.warner@materials.ox.ac.uk;

Abstract

Arrays of metal-semiconductor-metal (MSM) photodetectors are fabricated using chemical vapour deposition grown 2D monolayer WS₂ as the absorbing semiconductor (WS₂) with gold electrodes. A study of the channel length dependence (0.2-6.4 μm) on the photoresponsivity and gain show substantial increase in performance is achieved when the length is reduced down to 200nm. A large gain factor of up to 480 is measured for 200nm length devices and attributed to lowering of the Schottky barriers due to the filling of trapped states between the metal contact and WS₂ by photogenerated carriers. Only photoexcited carriers close to the interface contribute to filling trap states and lowering the Schottky barrier and therefore increasing channel length only adds series resistance to the device that reduces performance. These results reveal detailed insights regarding the mechanisms for photocurrent generation in lateral MSM photodetectors that employ CVD grown monolayer WS₂ material, which has important consequences for the commercial applications and large scale development of 2D imaging arrays.

KEYWORDS: Trapped state, MSM photodetector, TMDC, WS₂, Schottky barrier

2D materials have found application as photoabsorbers in ultrathin photodetectors, including graphene and transition metal dichalcogenides (TMDCs).^{[1] [2]} It is appealing to integrate 2D materials into circuits or other signal processors because of their space economy in vertical dimensions while being compatible with conventional lithography methods in the lateral dimensions. As the first discovered 2D material, graphene has been studied thoroughly and shown attractive properties like chemical inertia^[3], high carrier mobility^{[4] [5] [6]} and high strength^{[7] [8]}. In the case of photo detection, the semi-metal nature of graphene results a high dark current^{[1] [9]}, which is energetically unfavourable. A band gap is found in other 2D crystals with single elements like black phosphorus^[10], which is chemically unstable in ambient condition^{[10] [11]}. TMDCs represent another type of 2D material that is a layer of transition metal (like Mo, W) sandwiched between two layers of chalcogenide atoms (like S, Se, and Te)^[2]. Chemical vapour deposition (CVD) growth of TMDS has been realized recently^{[12] [13] [14] [15]}, which enables relative large scale production. TMDCs are relatively stable in atmospheric conditions and harsh environments^[16] which makes them competitive candidates for device applications without special protection. Monolayer TMDCs are direct band semiconductors^[2], which is ideal for high photon-electron conversion rates^{[17] [18]}. For example, WS₂ has a direct band-gap in the visible light region ($\sim 2\text{eV}$), accompanied by strong photo absorption of 5%-10% for a monolayer^[19].

Many types of photodetectors have been fabricated with 2D materials, with a general trend of reverse dependence on the photoresponse and band width. Graphene photodetectors with light absorbing quantum dots exhibit a photoresponsivity of around 10^8 A/W , and a slow response time of up to several seconds^[20]. On the other hand, the bandwidth of graphene photo detectors without a photo-gating layer can be wider than 1GHz, but the photoresponsivity is of the scale of mA/W ^{[21] [22]}. TMDC-based photodetectors exhibit diverse photoresponse behaviour. Ohmic contacts are generally assumed for Ti contacted TMDCs, which in turn leads to a small ratio of the photocurrent (I_{bright}) to

dark current (I_{dark}), ($I_{\text{bright}}/I_{\text{dark}}$)^{[23] [24]}. The photoresponsivity of TMDC based photodetector varies 9 orders of magnitude from the scale of $\mu\text{A/W}$ to kA/W , while the response time varies 3 orders of magnitude from the scale of ms to s^{[25] [26] [27] [28] [29]}. These large variations are due to a number of factors, such as input laser power, but clearly further detailed studies are needed to reveal more insights into the mechanisms behind photoconductors that utilize monolayer TMDCs.

Here, we fabricate and study the photoresponse of metal-semiconductor-metal (MSM) photodetectors built with CVD grown monolayer WS_2 . The large region of monolayer WS_2 grown by CVD opens the opportunity for fabricating large arrays of MSM photodetectors on one chip and the ability to explore the influence of device architecture such as channel length. Gold electrodes are used to form Schottky junctions between the metal contacts and semiconductor, required for a MSM photodetector.^[30] A Schottky barrier is formed using a high working function metal (e.g. Au) as the contact electrode and a semiconductor with higher Fermi level (e.g. n-type WS_2).^[31] The appearance of a Schottky barrier effectively limits the dark current to below the measurement limit of equipment in this experiment ($<10^{-11}$ A). The channel length is varied from 0.2 – 6.4 μm to explore how this affects the photoresponsivity and gain factors of the devices, with the aim of increasing device performance.

Results and Discussion

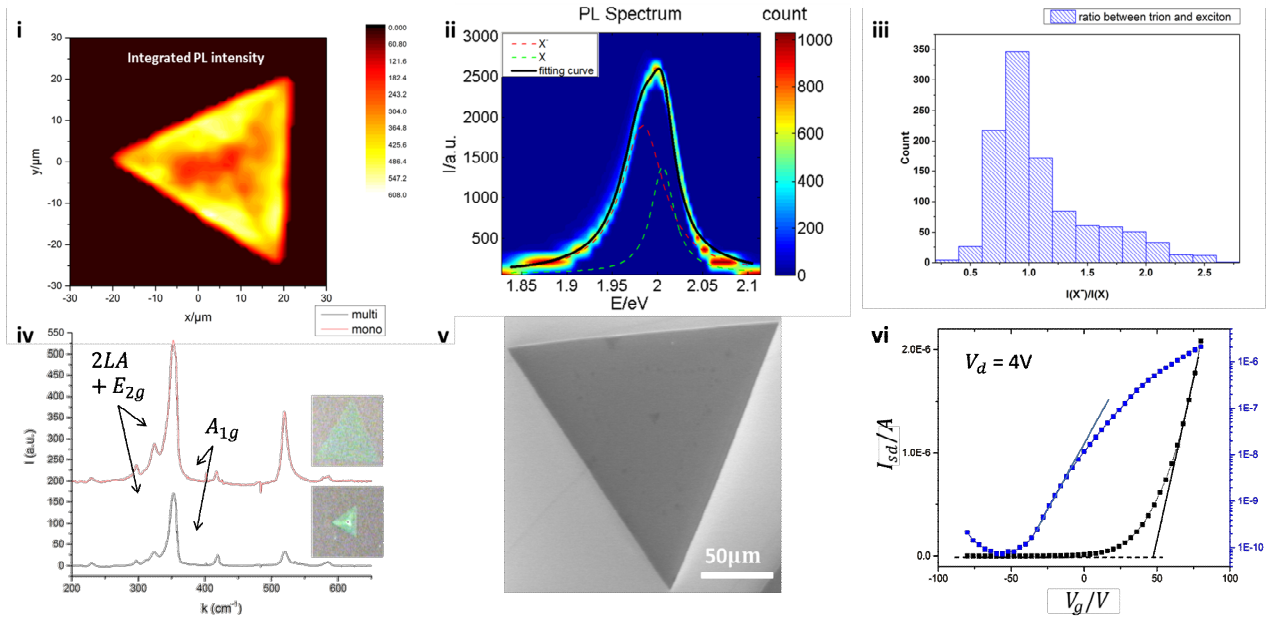


Figure 1 (i) Photoluminescence (PL) integrated intensity mapping of one WS₂ domain. PL intensity of monolayer WS₂ is much stronger than it in multilayer WS₂. The ratio between PL peak and Raman peak is used to identify the layer number of WS₂ in this work. (ii) Statistics of PL Spectrum of CVD-monolayer WS₂. The Colour bar in map represents the count of samples. Black solid line is the averaged PL spectrum of all samples, which splits into two peaks corresponding with trion (red dash line) and exciton (green dash line). (iii) Ratio between integrated intensity of trion and exciton. The ratio between these two peaks is proportion to the doping concentration as elaborated in the main text. (iv) Raman spectrum of CVD WS₂. The intensity ratio between (2LA+E_{2g}) peak and A_{1g} is used to confirm the layer number of WS₂. Insertions are the optical microscopic image of monolayer (above) and multilayer (below) WS₂. (v) SEM image of as-grown WS₂ domain. (vi) Transfer characteristics of a WS₂ field effect transistor (FET). The threshold voltage is 46V and field effect mobility is 4.2cm²/(Vs), which is determined by the intercept with I = 0 and slope of the black solid line respectively. The subthreshold swing (slope of blue line) is 17V/dec, which indicates a high density of trapped states.

The CVD WS₂ is grown directly onto Si wafers with 300nm oxide surface using a previously reported method with slight modification^[32]. The monolayer nature of the WS₂ triangular crystals in this work is confirmed by both photoluminescence (PL) and Raman spectroscopy. Single layer WS₂ domains emit much stronger PL than multi-layer domains due to their direct band gap^[33]. A typical PL intensity mapping from a monolayer WS₂ domain is shown in Figure 1(i). The ratio between the 2LA + E_{2g} and A_{1g} peaks in the Raman spectrum is another indicator of the layer number of the WS₂ crystal^[34]. The Raman spectrum shown in Figure 1 (iv) correlates with the PL analysis in terms of layer number. Some smaller multilayer domains of WS₂ are occasionally found, shown in the inset of figure 1(iv).

The PL spectrum is sensitive to the doping levels of WS₂ and statistics from over 1000 sample points are plotted in order to estimate the error in the PL measurement in Figure 1 (ii). The PL spectrum is repeatable and is well fitted by two peaks that correspond to trion (around 1.98eV) and exciton (around 2.02eV)^[35] emission. The significant trion peak in PL reflects an intrinsic doping in transferred CVD WS₂.^[35] ^[36] Such an intrinsic doping is possible to be caused by the transfer process^[37] or substrate^[38]. The doping concentration is further estimated by the ratio between spectral intensities of trion and exciton (Figure 1 (iii)) according to reference ^[35] and ^[36]:

$$\frac{N_X n_e}{N_{X^-}} = \left(\frac{16\pi m_X m_e}{h^2 m_{X^-}} \right) \frac{\exp(-\beta E_b)}{\beta} \quad (1)$$

$$\frac{I_{X^-}}{I_X} = \frac{\gamma_{X^-} N_{X^-}}{\gamma_X N_X} \quad (2)$$

where N_X is the population of exciton, N_{X^-} is the population of trion, n_e is the concentration of electron, m_X (or m_{X^-}) is the effective mass of exciton (or trion), m_e is the effective mass of electron, $\beta = \frac{1}{k_B T}$ is the Boltzmann factor, E_b is the binding energy, I_X (or I_{X^-}) is the integral

intensity of exciton (or trion), and γ_X (or γ_{X^-}) is the radiative decay rate of exciton (or trion). By fitting experimental data (**Figure 1** (ii)) with equations (1) and (2), we find an average doping concentration of $7 \times 10^{17} m^{-2}$, which is similar as previous reported value of WS₂.^[35]

The geometry of our MSM photo detectors is compatible with field effect transistor (FET) measurements to further characterize charge carrier mobility of the CVD WS₂. A typical transfer curve of a FETs with 6.4 μm channel length 4 μm channel width as **Figure 2** (iii,f) is presented in **Figure 1**(vi). These FETs display n-type behaviour and the threshold gate voltage is determined by the on-set of the conduction, as shown in Figure 1(vi). Field effect mobility is calculated according to the linear region of the transfer character:

$$\mu = \frac{dI_{sd}}{dV_g} \frac{L}{W} \frac{1}{V_{sd}C_i} \quad (3)$$

Here μ is the mobility, I_{sd} is the source-drain current, V_g is gate voltage, $\frac{L}{W}$ is the ratio between channel length and channel width, V_{sd} is the bias and C_i is the gate capacitance per unit area. The field effect mobility is determined as $4.2 cm^2/(Vs)$ from the slope of the linear region of transfer curve as shown in black line, Figure 1 (vi). This matches well with previous reported values of mobility in monolayer TMDs measured under ambient environment^{[39] [24]}. However, a significant subthreshold swing (17V/dec) is found in the field effect character of our CVD WS₂ (blue line in Figure 1(vi)) suggesting an abundance of trapped states^[40]. The density of trap states is extracted from the subthreshold swing using equation (4) ^[40]:

$$S = \frac{\ln 10}{e\beta} \left(1 + \frac{e^2}{C_i} N_{trap}\right) \quad (4)$$

Here S is subthreshold swing, $\beta = \frac{1}{k_B T}$ is the Boltzmann factor, e is the absolute value of single electron charge, C_i is the capacitance per unit area, N_{trap} is the trapped state density. The

subthreshold swing is measured by the slope of subthreshold region in the logarithmic plot of the transfer curve. We calculate a trap state density of $1.9 \times 10^{17} m^{-2} eV^{-1}$, which is similar to the surface state density reported in some 3D materials^{[31] [41]}, as well as in MoS₂ transistors^[42].

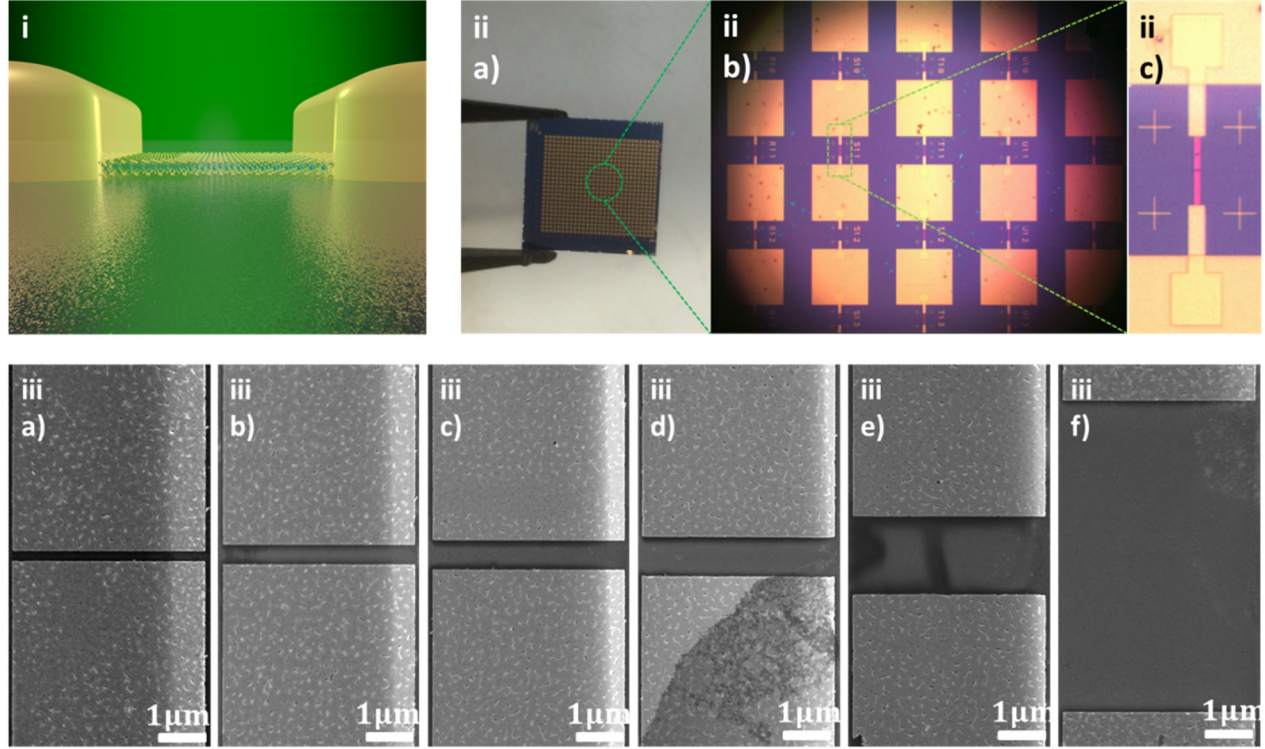


Figure 2 (i) Schematic illustration of a metal-semiconductor-metal (MSM) photodetector with monolayer WS₂ between two gold electrodes and 532nm laser illumination. (ii) a)–c) Optical images of devices on silicon chip. (ii) a) Photograph of the array of 24 x 17 devices on 1cm x 1cm silicon chip. (ii) b) Optical microscopic image of device lay-outs. (ii) c) Optical microscopic image of a pair of gold contacts. The pink colour of gold contact is due to the thin thickness (30nm) of them. The number of devices and pitch size is determined to optimize the possibility of contact sparsely distributed WS₂ on silicon chip. (iii) a)–f) Scanning electron microscopy (SEM) image of gold contacts on WS₂ with channel length varying from 200nm to 6400nm.

We fabricated metal-semiconductor-metal photodetectors using the CVD grown WS_2 with variations in the channel length. The WS_2 domains are transferred from the growth substrate onto a new substrate for device fabrication. Arrays of devices (24×17) are fabricated on the silicon chip with a pitch size of $300\mu\text{m}$ giving more than 400 photodetectors on one chip. The number of and pitch between devices are set to maximize the yield rate of working photodetectors. Optical images of the fabricated devices are shown in Figure 2 (ii) a)-c). Photodetectors with 6 different channel length, 200nm, 400nm, 600nm, 800nm, 1600nm and 6400 nm respectively, are fabricated, Figure 2 (iii) a)-f). The MSM photodetectors are tested with a 532nm laser with different intensity as schematically illustrated in Figure 2 (a). Only devices fabricated within a single triangular domain are characterized so as to rule out any influence of grain boundary.

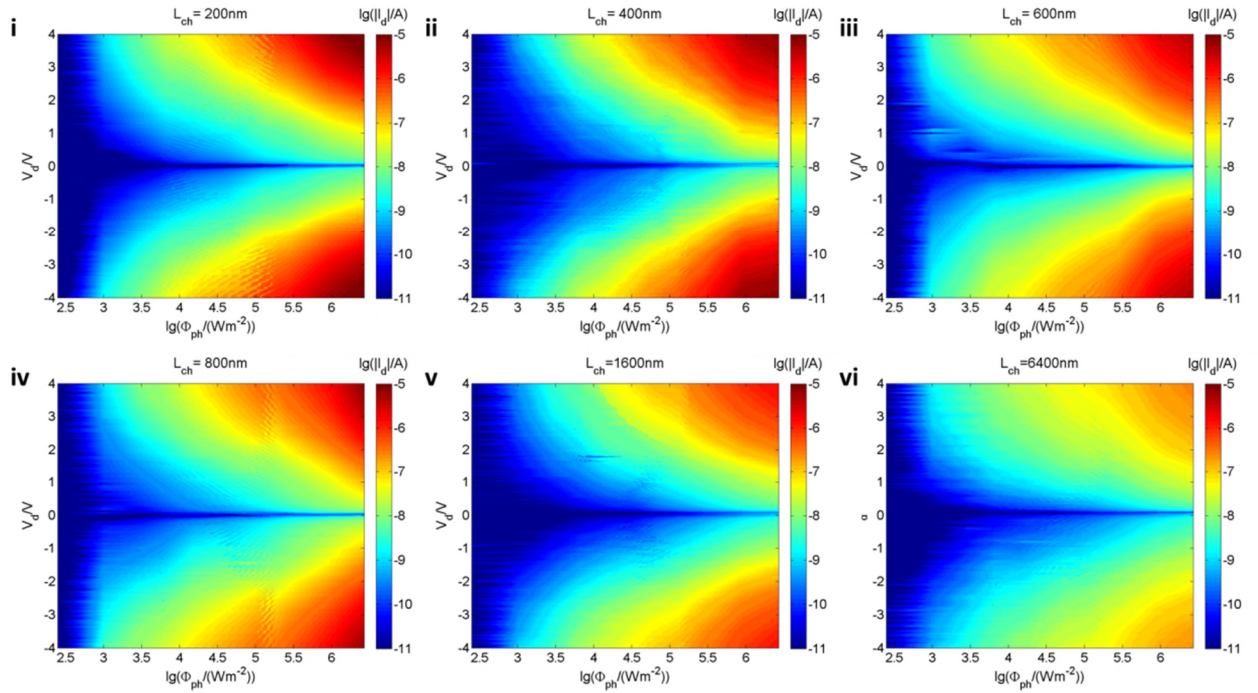


Figure 3. Maps of source-drain current in response to source-drain bias and incident laser intensity.

Colours in map (i) to (vi) represent absolute value of drain current in 10-based-logarithmic scale (as marked in the colour bar). The range of colour scale in all size maps is same (from 10pA to 10μA) for the convenience of comparison. X axis and Y axis are 10-based-logarithm of incident illumination intensity and source-drain bias respectively.

Photoresponse of devices with 6 different channel lengths (200nm, 400nm, 600nm, 800nm, 1600nm and 6400nm) were measured as a function of source-drain bias and incident light intensity as shown in Figure 3. The dark current is found to be lower than 10pA, which reaches the measurement limit of equipment used in this experiment. Due to the stable negligible dark current, we exclude the contribution of tunnelling current in our experimental set-up, which was reported in GaSe photodetectors with short channel lengths or high bias^[43]. Although the dark current remains almost undetectable no matter what channel length and source drain bias, the photocurrent sensitively depends on both. The maximum photocurrent, as can be found in the upper and lower right corner of each map, decreases with increasing channel length. Photocurrent at a given bias reaches the maximum value at the scale of 10μA in $\pm 4V$ biased 200nm-channel-length devices as shown in Figure 3 (i), while decreases to about 1% of that value in 6400nm-channel-length devices. Higher photoresponsivity for devices with shorter channel lengths and larger bias is found.

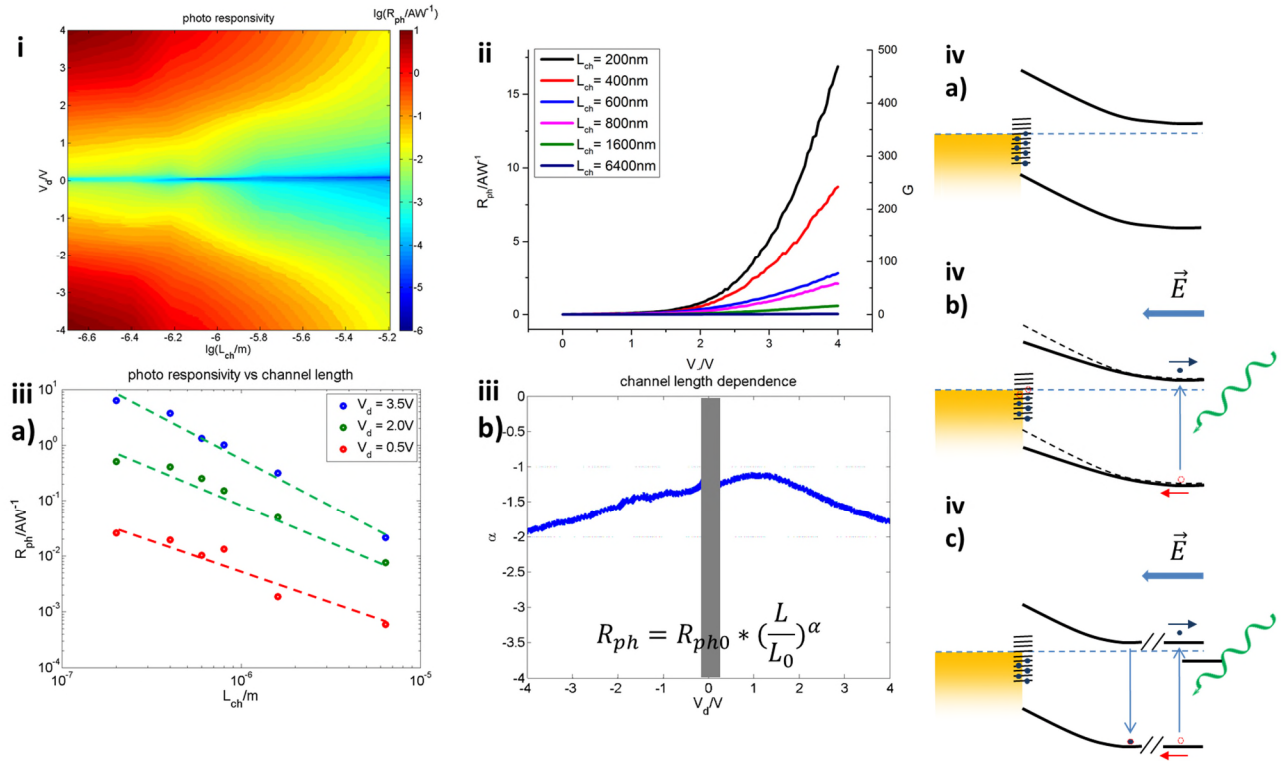


Figure 4 Photo responsivity of WS₂ MSM photodetector. (i) map of photo responsivity as a function of channel length and source-drain bias. Colours in the map represent the photo responsivity in 10-based-logistic scale as marked by the colour bar. The photo responsivity are tuned from $\sim 10^{-5}$ for long channel ($L_{ch} = 6400nm$) photo detectors working under low bias ($\sim 0.2V$) to $\sim 10^1$ for short channel ($L_{ch} = 200nm$) photodetector working under mild bias ($\sim 4V$). (ii) Dependence of photo responsivity (left y axis) and gain (right y axis) on source-drain bias. No current saturation is found for all devices, while gain higher than unity is found commonly. (iii) Dependence of photo responsivity on channel length. (iii,a) Dependence of photo responsivity on channel length with fitting lines. Relation between photo responsivity and channel length follows a power law with the power factor α varies with different source-drain voltage. (iii,b) Dependence of power factor α on source drain voltage. The α values near zero bias is masked due to noise induces by the small current value. (iv) Band diagram illustrating the photo response mechanism of WS₂ MSM photo detector. (iv,a) Trapped states exist at the interface between metal contact and WS₂. The trapped states will result a complicated Fermi level pinning effect and influence the effective Schottky barrier height. (iv,b) Photon absorption of the photo detector produces electron-hole pair. Holes are later trapped in the interface between metal contact and semiconductor, which decreases effective Schottky barrier height. The dashed lines indicate the origin position of the conduction and valence band while the solid lines are the actual position conduction and valence band after Fermi level lowering. (iv,c) When the channel length is comparable with the transient length of photo-induced electrons, recombination between electron and hole become significant.

Photoresponsivity and gain are two correlated figures of merit for photodetectors. Photoresponsivity measures the sensitivity of photodetector to incident light, which is defined as $R_{ph} = \frac{I_{ph}}{\Phi A}$, where R_{ph} is the photoresponsivity, I_{ph} is the photo current, Φ is the light intensity and

A is the detection area. The photoresponsivity of our WS₂ MSM photodetectors was found to be a function of both bias and channel length as in Figure 4(i). The photoresponsivity reaches up to 20A/W in for short channel lengths (200nm) and large source-drain bias (4V) (Figure 4 (ii)). Further increasing the bias above 4V will provide larger photoresponsivities, but in air we find the WS₂ begins to degrade when current values are too high and therefore we limit our study to 4V for consistency and reproducibility. Slightly smaller photoresponsivity has been reported in Au-MoS₂-Au photodetectors under similar illumination intensity^[16]. We note that the much stronger illumination (10^2W/m^2 - 10^6W/m^2) intensity in our experiment compared to some other reports (10^{-3}W/m^2 - 10^2W/m^2) would lead to an apparent smaller photoresponsivity due to the negative dependence of photoresponsivity on illumination intensity^[26]. The gain factor of a photo detector is defined as the number of charge carriers flowing through the circuit per photogenerated electron-hole pair^[44] and calculated by $G = \frac{h\nu}{e\eta} R_{ph}$, where G is the gain, R_{ph} is photo responsivity, h is plank constant, ν is the frequency of photon, e is the absolute value of electron charge, and η is the light absorption rate. By assuming an absorption rate of 8% for monolayer WS₂^[19], we calculated the gain factor to be as high as 480, Figure 4 (ii), which is similar to that found in conventional GaAs MSM photo detectors^{[45] [46] [47]} and organic photo detectors^[48].

The gain factor (and thus photoresponsivity) exponentially depends on the source-drain bias shown in Figure 4 (ii) due to the exponential dependence of emission current on the bias. Plot of $\log(R_{ph})$ vs $\log(L_{ch})$ reveals a power-law dependence of photoresponsivity on channel length, shown in Figure 4 (iii). The power factor varies from $\alpha = -2$, for high bias (4V) to $\alpha = -1$ for low bias as shown in Figure 4(iii,b). Under high bias, the current is limited by the internal resistance of materials. In this way, the initial photo current caused by the photogenerated electron hole pair is almost a fixed value but the gain changes according to the following formula^[44].

$$G = \frac{\mu_e + \mu_h}{\mu_e} \cdot \frac{\tau}{t_t} \quad (5)$$

$$t_t = \frac{L_{ch}^2}{\mu_e V} \quad (6)$$

Where in equation (5) and (6) G is the gain factor of the photo detector, μ_e and μ_h are the electron and hole mobility respectively, τ is the recombination life time, t_t is the transit time, which is the time for an electron to travel from one electrode to another, L_{ch} is the channel length, and V is the source-drain bias. From equation (5) and (6), it is clear that $G \propto L^{-2}$ (thus $R \propto G \propto L^{-2}$). On the other hand, if the source-drain bias is comparable or smaller than the effective Schottky barrier height, most voltage drops within the dipole layer between the WS_2 and gold contact. In this way, only electron-hole pairs that are generated within the depletion zone contribute to the photocurrent^[49]. Photocurrent is independent to channel length in that regime, which leads to the photoresponsivity depending reciprocally on the channel length (e.g. red line in Figure 4 (iii, a) and low bias region in Figure 4 (iii, b)). By taking our experimental data at high source-drain voltage into equation (5) and (6) and assuming that holes are trapped (i.e. $\mu_h \ll \mu_e$), we estimate the recombination life time to be around 7ns, which is similar as the theoretical prediction of radiative life time in monolayer WS_2 at ambient condition.^[50]

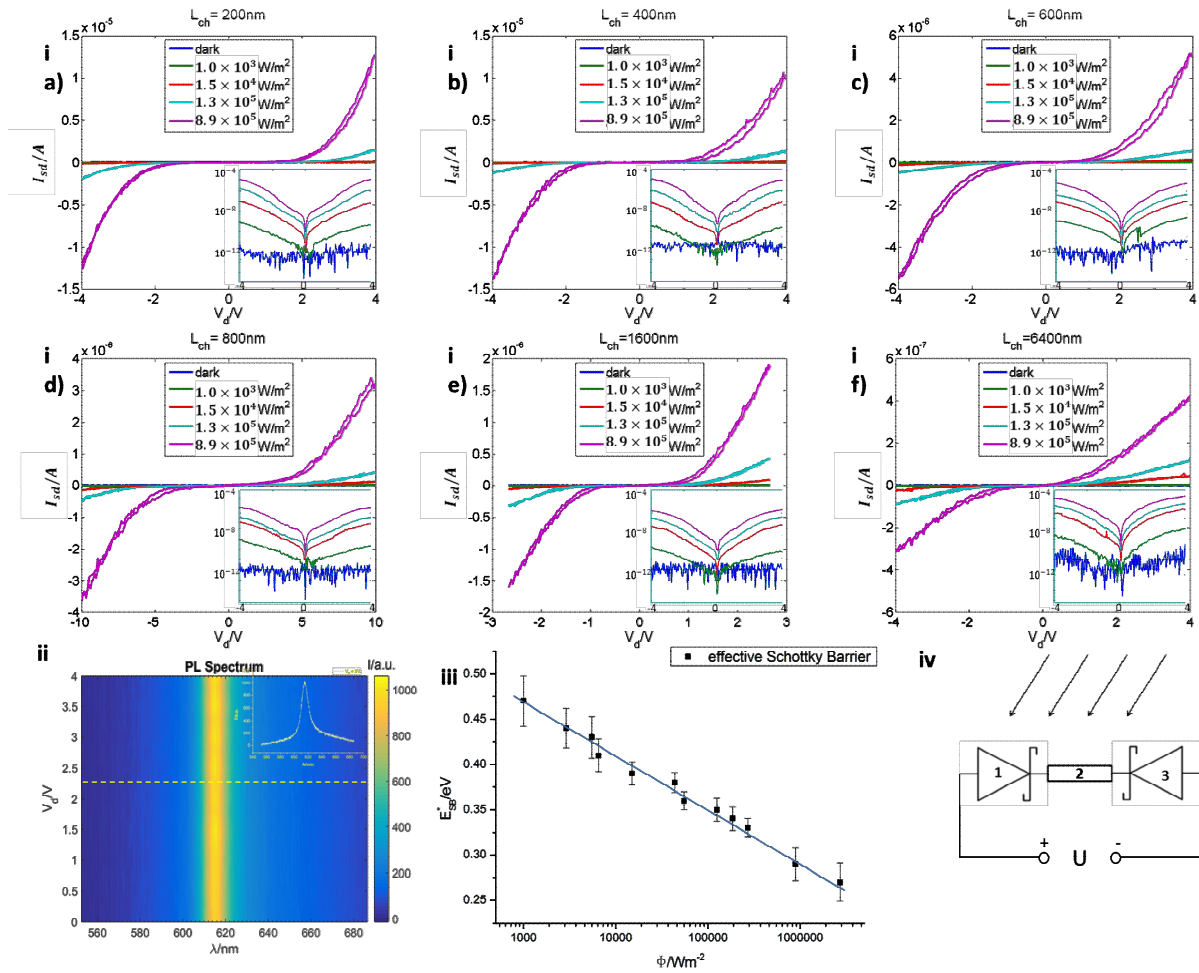


Figure 5. (i) a-f) Photoconductivity of WS₂ photodetectors for different channel lengths (200nm, 400nm, 600nm, 800nm, 1600nm and 6400nm). The insertions are IV plots in logarithmic scale. ^[51] (ii) PL spectrum of devices under different bias. Typical PL spectrum is shown as the insert that is taken at 2V bias (indicated by the yellow dashed line). (iii) Scatter plot of effective Schottky barrier height (E_{SB}) as a function of light intensity (Φ). The blue line is a fitting curve showing the linear dependence of effective Schottky barrier on logarithm of light intensity. (iv) Equivalent circuit diagram for a MSM photodetector. The MSM photodetector consists of a pair of back-to-back Schottky diodes (device 1, 3) and a series resistor (device 2).

To further clarify the photoresponse mechanisms for the Au-WS₂-Au MSM photodetector, the output character is carefully studied. Non-linear IV curves appear as the output character of all devices. Typical IV curves of devices with various channel lengths are shown in Figure 5(i) a-f).

These non-linear IV curves indicate the formation of a Schottky barrier^{[52] [53]}, which is desirable in MSM photo detector. We model the output character as an electrical circuit consisting of two Schottky diodes contacted back-to-back with a series resistance in the middle (insert of Figure 5 (1), a)-f)). For small source-drain bias, the reverse-biased diode limits the current flow through the circuit. When increasing the bias, leakage through the reverse-biased diode becomes significant and current flows through the circuit with an exponential increase. Several mechanisms, e.g. increasing of field emission^[54], minority carrier injection^[55] or avalanche break-down of the channel material^[55], may result in similar non-linear IV curves in the set of back-to-back diodes in Figure 5 (i).

Avalanche break-down is reported in 2D avalanche photodetectors^[56], but is unlikely to occur in our experimental conditions. The electric field should strongly alter the PL spectrum^[57] when avalanche break-down happens. However, the PL spectrum remains almost unchanged in our experiments as shown in Figure 5 (ii). In addition, when avalanche break-down occurs, the kinetic energy of charge carriers is approximately equal to the band gap^[58]. We can roughly estimate the kinetic energy by $E_k \sim \frac{1}{2} m^* \left(\frac{\mu V_{sd}}{L_{ch}} \right)^2$, where E_k is the kinetic energy, m^* is the effective mass, μ is the mobility, V_{sd} is the source-drain bias, L_{ch} is the channel length. Even though the kinetic energy estimated in this way ($\sim 1\text{meV}$) is generally larger than the real kinetic energy, it is still three orders of magnitude smaller than the band gap of WS_2 ($\sim 2\text{eV}$).

By ruling out avalanche break-down, we can describe the output character of the photoresponse using a modified theory for thermionic emission current. The contribution of other transport mechanisms (field emission and minority carrier injection) is considered by adding a phenomenological ideality factor^[59]. Due to the large gain in our experiment (Figure 4(ii)), the total current is almost totally contributed by the thermionic emission current. In this way, we can describe

the current flowing through the back-to-back Schottky diode pair as a series resistance by the following set of equations^{[60] [61]}:

$$I = I_0 \exp\left(-\left(1 - \frac{1}{n}\right)e\beta V_1\right) (\exp(e\beta V_1) - 1) \quad (7)$$

$$I = \frac{V_2}{R} \quad (8)$$

$$I = -I_0 \exp\left(\left(1 - \frac{1}{n}\right)e\beta V_3\right) (\exp(-e\beta V_3) - 1) \quad (9)$$

$$U = V_1 + V_2 + V_3 \quad (10)$$

Where, in equations (7)-(10), I is the source-drain current, U is the source-drain bias, I_0 is a constant determined by the Schottky barrier height, n is the ideality factor, e is the absolute value of single electron charge, $\beta = \frac{1}{k_B T}$ is the Boltzmann factor, and V_i ($i = 1, 2, 3$) are the voltage drop across device 1 (diode on the left), 2 (resistor in the middle) and 3 (diode on the right) in figure 5(iv) respectively. By solving equations (7)-(10), we get:

$$I = I_0 \left[\frac{\cosh\left(\frac{1}{2}\left(1 - \frac{1}{n}\right)e\beta(U - IR)\right)}{\cosh\left(\frac{1}{2n}e\beta(U - IR)\right)} \right]^{-\left(1 - \frac{1}{n}\right)} \cdot \frac{\sinh\left(\frac{1}{2}e\beta(U - IR)\right)}{\cosh\left(\frac{1}{2n}e\beta(U - IR)\right)} \quad (11)$$

Notations in the equation (11) share the same meaning as in equations (7)-(10). By fitting the measured IV curve with the equation (11), can we extract the pre-factor I_0 , internal resistance R and ideality factor n . Especially, I_0 is determined by the Schottky barrier height of the 1D junction between metal contact and 2D WS₂^{[62] [63]}.

$$I_0 = wA_{2D}^*T^{3/2}\exp(-\beta e\phi_{SB}^*) \quad (12)$$

Where in equation (12), S is the contact area, A^* is the effective 2D Richardson constant, T is temperature, $\beta = \frac{1}{k_B T}$ is the Boltzmann factor, and ϕ_{SB}^* is the effective Schottky barrier height. By taking the fitting parameter I_0 into equation (12), we can calculate the effective Schottky barrier height in the WS_2 MSM photo detector, which is plotted in Figure 5 (iii).

Both the ideality factor and the Schottky barrier height are extracted by fitting the experimental data to formulas above. The ideality factor is around 1.03 ± 0.01 , which is near unity and thus indicates ideal Schottky junctions are formed between WS_2 and the gold contact. This value is consistence with common diodes and transistors. It is notable that the effective barrier depends negatively on the incident light intensity, but has no correlation with the channel length down to 200nm in our experiment. This suggests a very narrow depletion zone in our device, which is likely due to an abundancy of trapped state in the interface between electrode and WS_2 .

The lowering of the effective Schottky barrier height can be understood as a result of accumulating trapped charge at the interface between the metal contact and semiconductor.⁴⁹ The hysteresis in Figure 5 (i) is due to the charge and discharge process of trapped states in the interface between electrode and WS_2 . Incident light can generate electron-hole pairs, which are separated by the external electric field. Although electrons can easily drift to and enter the positive electrode (anode), holes are trapped in the interface between the negative electrode (cathode) and semiconductor, especially if there is an abundancy of trapped states. The semiconductor is then going to be positively charged around the cathode due to the accumulation of holes. These charges in turn lower the local Fermi level of WS_2 , which further decreases the Schottky barrier height. Such a mechanism is schematically plotted in Figure 4 (iv,b). Similar photo induced trapped charge accumulation is

reported in graphene-MoS₂ interfaces acting as a photo gate^[64]. When reaching equilibrium, the Schottky barrier height decreases to such a level that electrons can be injected into the WS₂ by thermionic emission and the holes no longer accumulate near the positive electrode. Similar mechanisms have successfully explained the gain in GaAs MSM photodetectors^{[45] [46] [47]}.

Conclusion

We have revealed that filling trapped states at the interface between gold contacts and WS₂ leads to a lowering of effective Schottky barrier height, enabling current injection from the electrodes to dominate. A large gain factor (as high as 480) and small dark current (smaller than 10pA) is realized with mild bias (4V) without any gate for small channel length devices (200nm). Channel length dependence shows that smaller channels give higher photoconductivity and future devices should utilize this advantage to eliminate series resistance effects of the central WS₂ region that has limited role in contributing to the photocurrent activation mechanism. Photo sensing unit with smaller channel length can further lead to a higher packing density in one chip, which will provide better resolution. The large area growth of WS₂ monolayers enabled arrays of photodetectors to be fabricated and opens up the opportunity to produce 2D imaging sensors.

Methods

CVD growth of WS₂

WS₂ is synthesized with a two furnace system to control the temperature of S and WO₃ separately. A 2×2 cm² silicon chip with 300nm SiO₂ on top was used as the growth substrate. The substrate is cleaned then loaded into the reaction furnace together with precursors. 300 mg sulfur powder (≥99.5%, Sigma-Aldrich) and 200mg WO₃ is used for synthesis. The position and distance between precursors and substrate are carefully controlled so as to grow monolayer WS₂. Before CVD growth,

the system is flushed with 500 sccm Argon for at least 30min to remove the air inside. WO_3 is heated up to 1170 °C and S to 180 °C for the reaction. The reaction lasts for 3 min with a carrier gas (Ar) flowing at 250 sccm. When finishing the reaction, we decrease the temperature of WO_3 quickly, while heating S to 450 °C to deplete the unreacted S. WS_2 is transferred from the growth substrate to the device substrate using a PMMA scaffold and etching the SiO_2 in KOH to detach from the substrate. PMMA was removed by a hot acetone bath for 2hrs.

Device fabrication

We first fabricate an array of large Au contact pads ($150\mu\text{m} \times 150\mu\text{m}$) on the 1cm^2 chip by conventional resist based e-beam lithography as the first step. Then the WS_2 is transferred on to the chip containing the contact pads. The WS_2 domains are located randomly on the chip with a certain amount of them falling in the middle region between the large contact pads. A second e-beam lithography step is carried out to fabricate fine Au contacts that connect to the WS_2 domains. The WS_2 is then patterned in to $4\mu\text{m} \times 20\mu\text{m}$ ribbons by another e-beam lithography and oxygen plasma etching.

Photoconductivity measurements

All measurement is carried out in ambient conditions at room temperature. A Keithley 2401 semiconductor parameter analyser is used for all electronic measurements. A 532nm laser source is used as the illumination source by coupling into a confocal microscope system to focus the laser to a spot size of $138\mu\text{m}^2$, which is much larger than the largest detection area (e.g. $L_{\text{ch}}=6.4\mu\text{m}$ and $W_{\text{ch}}=4\mu\text{m}$, and thus $\sim 25\mu\text{m}^2$ detection area) and provides relatively uniform illumination.

Acknowledgements

YF thanks the Clarendon Fund, Oxford, for support. JHW thanks the Royal Society and Samsung for support.

References

- [1] F. H. L. Koppens, T. Mueller, P. Avouris, A. C. Ferrari, M. S. Vitiello, M. Polini, *Nat. Nanotechnol.* **2014**, *9*, 780.
- [2] Q. H. Wang, K. Kalantar-Zadeh, A. Kis, J. N. Coleman, M. S. Strano, *Nat. Nanotechnol.* **2012**, *7*, 699.
- [3] S. Chen, L. Brown, M. Levendorf, W. Cai, S.-Y. Ju, J. Edgeworth, X. Li, C. W. Magnuson, A. Velamakanni, R. D. Piner, J. Kang, J. Park, R. S. Ruoff, *ACS Nano* **2011**, *5*, 1321.
- [4] S. V. Morozov, K. S. Novoselov, M. I. Katsnelson, F. Schedin, D. C. Elias, J. A. Jaszczak, A. K. Geim, *Phys. Rev. Lett.* **2008**, *100*, 016602.
- [5] C. R. Dean, a F. Young, I. Meric, C. Lee, L. Wang, S. Sorgenfrei, K. Watanabe, T. Taniguchi, P. Kim, K. L. Shepard, J. Hone, *Nat. Nanotechnol.* **2010**, *5*, 722.
- [6] N. Petrone, C. R. Dean, I. Meric, A. M. van der Zande, P. Y. Huang, L. Wang, D. Muller, K. L. Shepard, J. Hone, *Nano Lett.* **2012**, *12*, 2751.
- [7] C. Lee, X. Wei, J. W. Kysar, J. Hone, *Science* **2008**, *321*, 385.
- [8] A. K. Geim, K. S. Novoselov, *Nat. Mater.* **2007**, *6*, 183.
- [9] F. Bonaccorso, Z. Sun, T. Hasan, a C. Ferrari, *Nat. Photonics* **2010**, *4*, 611.
- [10] L. Li, Y. Yu, G. J. Ye, Q. Ge, X. Ou, H. Wu, D. Feng, X. H. Chen, Y. Zhang, *Nat. Nanotechnol.* **2014**, *9*, 372.
- [11] J. D. Wood, S. A. Wells, D. Jariwala, K. Chen, E. Cho, V. K. Sangwan, X. Liu, L. J. Lauhon, T. J. Marks, M. C. Hersam, *Nano Lett.* **2014**, *14*, 6964.
- [12] Y. Zhang, Y. Zhang, Q. Ji, J. Ju, H. Yuan, J. Shi, T. Gao, D. Ma, M. Liu, Y. Chen, X. Song, H. Y. Hwang, Y. Cui, Z. Liu, *ACS Nano* **2013**, *7*, 8963.
- [13] Y. H. Lee, X. Q. Zhang, W. Zhang, M. T. Chang, C. Te Lin, K. Di Chang, Y. C. Yu, J. T. W. Wang, C. S. Chang, L. J. Li, T. W. Lin, *Adv. Mater.* **2012**, *24*, 2320.
- [14] H. Zhou, C. Wang, J. C. Shaw, R. Cheng, Y. Chen, Y. Liu, N. O. Weiss, Z. Lin, Y. Huang, X. Duan, *Nano Lett.* **2014**, *15*, 709.
- [15] Y. Shi, H. Li, L. Li, *Chem. Soc. Rev.* **2015**, *44*, 2744.
- [16] D. S. Tsai, K. K. Liu, D. H. Lien, M. L. Tsai, C. F. Kang, C. A. Lin, L. J. Li, J. H. He, *ACS Nano* **2013**, *7*, 3905.
- [17] L. Britnell, R. M. Ribeiro, a Eckmann, R. Jalil, B. D. Belle, a Mishchenko, Y.-J. Kim, R. V Gorbachev, T. Georgiou, S. V Morozov, a N. Grigorenko, a K. Geim, C. Casiraghi, a H. Castro Neto, K. S. Novoselov, *Science* **2013**, *340*, 1311.
- [18] W. J. Yu, Y. Liu, H. Zhou, A. Yin, Z. Li, Y. Huang, X. Duan, *Nat. Nanotechnol.* **2013**, *8*, 952.
- [19] M. Bernardi, M. Palummo, J. C. Grossman, *Nano Lett.* **2013**, *13*, 3664.

- [20] G. Konstantatos, M. Badioli, L. Gaudreau, J. Osmond, M. Bernechea, F. P. G. de Arquer, F. Gatti, F. H. L. Koppens, *Nat. Nanotechnol.* **2012**, 7, 363.
- [21] T. Mueller, F. Xia, P. Avouris, *Nat. Photonics* **2010**, 4, 297.
- [22] F. Xia, T. Mueller, Y.-M. Lin, A. Valdes-Garcia, P. Avouris, *Nat. Nanotechnol.* **2009**, 4, 839.
- [23] O. Lopez-Sanchez, D. Lembke, M. Kayci, A. Radenovic, A. Kis, *Nat. Nanotechnol.* **2013**, 8, 497.
- [24] N. Huo, S. Yang, Z. Wei, S.-S. Li, J.-B. Xia, J. Li, *Sci. Rep.* **2014**, 4, 5209.
- [25] C. Lan, C. Li, Y. Yin, Y. Liu, *Nanoscale* **2015**, 7, 5974.
- [26] N. Perea-López, A. L. Elías, A. Berkdemir, A. Castro-Beltran, H. R. Gutiérrez, S. Feng, R. Lv, T. Hayashi, F. López-Urías, S. Ghosh, B. Muchharla, S. Talapatra, H. Terrones, M. Terrones, *Adv. Funct. Mater.* **2013**, 23, 5511.
- [27] W. Choi, M. Y. Cho, A. Konar, J. H. Lee, G. B. Cha, S. C. Hong, S. Kim, J. Kim, D. Jena, J. Joo, S. Kim, *Adv. Mater.* **2012**, 24, 5832.
- [28] O. Lopez-Sanchez, D. Lembke, M. Kayci, A. Radenovic, A. Kis, *Nat. Nanotechnol.* **2013**, 8, 497.
- [29] W. Zhang, J. K. Huang, C. H. Chen, Y. H. Chang, Y. J. Cheng, L. J. Li, *Adv. Mater.* **2013**, 25, 3456.
- [30] P. R. Berger, *IEEE Potentials* **1996**, 15, 25.
- [31] A. M. Cowley, S. M. Sze, *J. Appl. Phys.* **1965**, 36, 3212.
- [32] Y. Rong, Y. Fan, A. Leen Koh, A. W. Robertson, K. He, S. Wang, H. Tan, R. Sinclair, J. H. Warner, *Nanoscale* **2014**, 6, 12096.
- [33] H. R. Gutierrez, N. Perea-Lopez, A. L. Elias, A. Berkdemir, B. Wang, R. Lv, F. Lopez-Urias, V. H. Crespi, H. Terrones, M. Terrones, *Nano Lett.* **2013**, 13, 3447.
- [34] A. Berkdemir, H. R. Gutiérrez, A. R. Botello-Méndez, N. Perea-López, A. L. Elías, C.-I. Chia, B. Wang, V. H. Crespi, F. López-Urías, J.-C. Charlier, H. Terrones, M. Terrones, *Sci. Rep.* **2013**, 3, 1755.
- [35] N. Peimyoo, W. Yang, J. Shang, X. Shen, Y. Wang, T. Yu, *ACS Nano* **2014**, 8, 11320.
- [36] S. Mouri, Y. Miyauchi, K. Matsuda, *Nano Lett.* **2013**, 13, 5944.
- [37] Z. Xu, Y. Zhang, S. Lin, C. Zheng, Y. L. Zhong, X. Xia, Z. Li, P. J. Sophia, M. S. Fuhrer, Y. Cheng, Q. Bao, **2015**, 6178.
- [38] Y. Kobayashi, S. Sasaki, S. Mori, H. Hibino, Z. Liu, K. Watanabe, T. Taniguchi, K. Suenaga, Y. Maniwa, Y. Miyata, *ACS Nano* **2015**, 9, 4056.
- [39] D. Ovchinnikov, A. Allain, Y. Huang, D. Dumcenco, A. Kis, *ACS Nano* **2014**, 8, 8174.
- [40] F. Najam, M. L. P. Tan, R. Ismail, Y. Seop Yu, *Semicond. Sci. Technol.* **2015**, 30, 075010.
- [41] S. G. Louie, J. R. Chelikowsky, M. L. Cohen, *Phys. Rev. B* **1977**, 15, 2154.
- [42] S. Ghatak, A. N. Pal, A. Ghosh, *ACS Nano* **2011**, 5, 7707.
- [43] Y. Cao, K. Cai, P. Hu, L. Zhao, T. Yan, W. Luo, X. Zhang, X. Wu, K. Wang, H. Zheng, *Sci. Rep.* **2015**, 5, 8130.

- [44] B. E. A. Saleh, M. C. Teich, In *Fundamentals of Photonics*; Wiley Series in Pure and Applied Optics; John Wiley & Sons, Inc.: New York, USA, 1991.
- [45] T. Sugeta, T. Urisu, S. Sakata, Y. Mizushima, *Jpn. J. Appl. Phys.* **1980**, *19*, 459.
- [46] Y. K. Su, S. J. Chang, C. H. Chen, J. F. Chen, G. C. Chi, J. K. Sheu, W. C. Lai, J. M. Tsai, *IEEE Sens. J.* **2002**, *2*, 366.
- [47] O. Katz, V. Garber, B. Meyler, G. Bahir, J. Salzman, *Appl. Phys. Lett.* **2001**, *79*, 1417.
- [48] C. Dye, H. Zhang, S. Jenatsch, J. De Jonghe, F. Nu, R. Hany, **2015**, *1*.
- [49] C. C. Wu, D. Jariwala, V. K. Sangwan, T. J. Marks, M. C. Hersam, L. J. Lauhon, *J. Phys. Chem. Lett.* **2013**, *4*, 2508.
- [50] M. Palummo, M. Bernardi, C. Grossman, **2015**.
- [51] A. Sawa, T. Fujii, M. Kawasaki, Y. Tokura, *Appl. Phys. Lett.* **2013**, *4073*, 12.
- [52] J. Chen, P. M. Odenthal, A. G. Swartz, G. C. Floyd, H. Wen, K. Y. Luo, R. K. Kawakami, *Nano Lett.* **2013**, *13*, 3106.
- [53] S. Tans, A. Verschuere, C. Dekker, *Nature* **1998**, *672*, 669.
- [54] F.A.Padovani, R.Stratton, *Solid. State. Electron.* **1966**, *9*, 695.
- [55] S. M. Sze, D. J. Coleman, a. Loya, *Solid. State. Electron.* **1971**, *14*, 1209.
- [56] S. Lei, F. Wen, L. Ge, S. Najmaei, A. George, Y. Gong, W. Gao, Z. Jin, B. Li, J. Lou, J. Kono, R. Vajtai, P. Ajayan, N. J. Halas, *Nano Lett.* **2015**, *15*, 3048.
- [57] S. Tasch, G. Kranzelbinder, G. Leising, U. Scherf, *Phys. Rev. B* **1997**, *55*, 5079.
- [58] S.O. Kasap, In *Optoelectronics and photonics :principles and practices*; Gilfillan, A.; Dworkin, A., Eds.; Pearson Education, Inc., 2012.
- [59] E. H. Rhoderick, *IEE Proc. I Solid State Electron Devices* **1982**, *129*, 1.
- [60] A. J. Chiquito, C. a Amorim, O. M. Berengue, L. S. Araujo, E. P. Bernardo, E. R. Leite, *J. Phys. Condens. Matter* **2012**, *24*, 225303.
- [61] Y. Ohta, Y. Kubozono, A. Fujiwara, *Appl. Phys. Lett.* **2008**, *92*, 173306.
- [62] J. Chen, P. M. Odenthal, A. G. Swartz, G. C. Floyd, H. Wen, K. Y. Luo, R. K. Kawakami, A. J. Chiquito, C. a Amorim, O. M. Berengue, L. S. Araujo, E. P. Bernardo, E. R. Leite, F.A.Padovani, R.Stratton, F. Hernández-Ramírez, A. Tarancón, O. Casals, J. Rodríguez, A. Romano-Rodríguez, J. R. Morante, S. Barth, S. Mathur, T. Y. Choi, D. Poulikakos, V. Callegari, P. M. Nellen, Y. Ohta, Y. Kubozono, A. Fujiwara, E. H. Rhoderick, S. M. Sze, D. J. Coleman, a. Loya, A. Anwar, B. Nabet, J. Culp, F. Castro, *Solid. State. Electron.* **2013**, *24*, 695.
- [63] W. Liu, D. Sarkar, J. Kang, W. Cao, K. Banerjee, *ACS Nano* **2015**, *9*, 7904.
- [64] W. Zhang, C.-P. Chuu, J.-K. Huang, C.-H. Chen, M.-L. Tsai, Y.-H. Chang, C.-T. Liang, Y.-Z. Chen, Y.-L. Chueh, J.-H. He, M.-Y. Chou, L.-J. Li, *Sci. Rep.* **2014**, *4*, 1.

TOC graphic

